Article:
Smyl, D., Hallaji, M., Seppanen, A. et al. (2016) Quantitative electrical imaging of three-dimensional moisture flow in cement-based materials. International Journal of Heat and Mass Transfer, 103. pp. 1348-1358. ISSN: 0017-9310

https://doi.org/10.1016/j.ijheatmasstransfer.2016.08.039

Quantitative Electrical Imaging of Three-Dimensional Moisture Flow in Cement-Based Materials

Danny Smyl[a], Milad Hallaji[b], Aku Seppänen[c], Mohammad Pour-Ghaz[a,*]

[a] *North Carolina State University, Department of Civil, Construction, and Environmental Engineering, Campus Box 7908, 431C Mann Hall, Raleigh, NC 27695-7908*
[b] *WSP USA, 512 7th Avenue, New York, NY 10018*
[c] *Department of Applied Physics, University of Eastern Finland, PO Box 1627, Kuopio, Finland FI-70211*

Abstract

The presence of moisture significantly affects the mechanical, hydraulic, chemical, electrical, and thermal properties of cement-based and other porous materials, and therefore, methods for detecting and quantifying the moisture ingress in these materials are needed. Recent research studies have shown that the ingress of moisture in porous materials can be *qualitatively* imaged with Electrical Impedance Tomography (EIT) – an imaging modality which uses electrical measurements from object's surface to reconstruct the electrical conductivity distribution inside the object. The aim of this study is to investigate whether EIT could image the three-dimensional volumetric moisture content within cement-based materials *quantitatively*. For this aim, we apply the so-called absolute imaging scheme to the EIT image reconstruction, and use an experimentally developed model for converting the electrical conductivity distribution to volumetric moisture content. The results of the experimental studies support the feasibility of EIT for quantitative imaging of three-dimensional moisture flows in cement-based materials.

Keywords: Electrical Impedance Tomography (EIT), Imaging, Non-destructive testing, Unsaturated Moisture Flow, X-ray imaging, Cement-based materials.

1. Introduction

The mechanical, hydraulic, chemical, thermal, and electrical properties of porous media are significantly affected by the moisture content within the media [1, 2, 3], and especially in cement-based materials, the majority of deterioration processes take place in the presence of moisture [4, 5, 6]. For these reasons, there has been a significant interest in developing methods of monitoring moisture flows in cement-based materials and other porous media. While some high-resolution imaging methods of monitoring moisture flow in porous media are available, e.g. X-ray imaging [7, 8, 9, 10], γ-rays [11, 12, 13], neutron imaging [14, 15, 16, 17, 18, 19, 20, 21, 22, 23], and nuclear magnetic resonance [24, 25, 26, 27, 28], these methods are often expensive, limited to testing small specimens, and/or have significant energy demand. Electrically-based methods, on the other hand, have often a limited spatial resolution but are generally inexpensive, non-invasive, and require comparatively lower energy [29, 30, 31, 32, 33, 34, 35]. One electrically-based method that has been recently shown to be particularly promising for monitoring moisture in porous media is Electrical Impedance Tomography (EIT) [36, 15, 37].

In EIT, the electrical conductivity distribution inside an object is reconstructed based on voltage measurements from the surface of the object. Previous studies have demonstrated the feasibility of EIT to *qualitatively* image unsaturated moisture flows in porous media. Such research includes: 1D and 2D unsaturated moisture flow in soil [38, 39, 40, 41] and cement-based material [42, 43, 37, 15], as well as 3D moisture flow in sand [44], sandstone [45], soil [46] and cement-based materials [36]. In all these works, (the spatial map of) the increase of the moisture content with respect to some initial state was inferred qualitatively

*Corresponding author
Email address: mpourghaz@ncsu.edu (Mohammad Pour-Ghaz)

Nomenclature

α	van Genuchten model fitting parameter
$\bar{n}$	unit normal vector
ℓ	arc length variable
Γ_{e}	covariance matrix
μ	X-ray attenuation coefficient
μ_{air}	X-ray attenuation coefficient of air
μ_{water}	X-ray attenuation coefficient of water
Ω	target volume
$\partial\Omega$	target boundary
ρ	electrical resistivity
ρ_{w}	density of water
σ	electrical conductivity
$\sigma_{\max}$	upper constraint of electrical conductivity
$\sigma_{\min}$	lower constraint of electrical conductivity
Θ	effective material saturation
θ	volumetric moisture content
θ_{i}	initial volumetric moisture content
θ_{r}	residual volumetric moisture content
θ_{s}	volumetric moisture content at saturation
$\widehat{\sigma}$	conductivity estimate
ξ_l	contact impedance of l^{th} electrode
A	specimen cross-sectional area
d	X-ray specimen width
e	Gaussian distributed noise
e_l	l^{th} electrode
H	Hounsfield number for unsaturated material
h	capillary pressure
H_{s}	Hounsfield number for saturated material
I	tortuosity and pore connectivity parameter
I_0	intensity of incident X-ray
I_{x}	intensity of transmitted X-ray
I_l	total current of l^{th} electrode
K	unsaturated hydraulic conductivity
K_{r}	relative hydraulic conductivity
K_{s}	saturated hydraulic conductivity
L	specimen length
L_{e}	Cholesky factor for the noise precision matrix
L_σ	Spatially weighted discrete differential operator
m	van Genuchten model fitting parameter
m_{w}	molecular weight of water
n	van Genuchten model fitting parameter
$p(\sigma)$	regularization function
R	electrical resistance
R_{s}	universal gas constant
RH	relative humidity
T	temperature
U	EIT forward mapping
u	electric potential
U_l	electrode potential
V	measured electrode potentials
w/c	water to cement ratio
x, y, z	spatial coordinates

from a relative increase in the electrical conductivity (or decrease in the electrical resistivity) distribution. The change in the electrical conductivity was estimated using a linear approximation in the solution of the the non-linear EIT inverse problem, i.e., using the so-called *linearized difference imaging* scheme, resulting in a qualitative estimation of the conductivity change [15].

The aim of this study is to investigate whether EIT could be used for *quantitative* estimation of the three-dimensionally distributed water content in cement-based materials. In the experiments, moisture ingresses cement-based material containing fine aggregates. EIT measurements are collected during the moisture ingress, and used for reconstructing the 3D distribution of the electrical conductivity within the material. For the EIT reconstruction, the so-called *absolute imaging* scheme [47, 48, 49, 50] is adopted. The reconstructed electrical conductivity distributions are further converted to volumetric moisture content distributions, by using an experimentally-developed model. The results of EIT are compared with X-ray

Computed Tomography (CT) and numerical simulations of unsaturated moisture flow. While the experiments are performed on cement-based materials, the methods developed in this work are also applicable to other porous materials.

2. Materials

2.1. General

For testing the feasibility of EIT for monitoring the moisture ingress in cement-based materials, two cylindrical mortar specimens were prepared. In the experiments, the moisture was added to the specimen from a PVC reservoir mounted on top of the specimen (Fig. 1). In one specimen, the reservoir was filled with water and in the second specimen, dilute solution of water and non-ionic radiocontrast agent (Iohexol, 120 mg Iodine/ml) was used. This was done to improve the contrast between the background and the regions of moisture ingress in X-ray CT imaging [36].

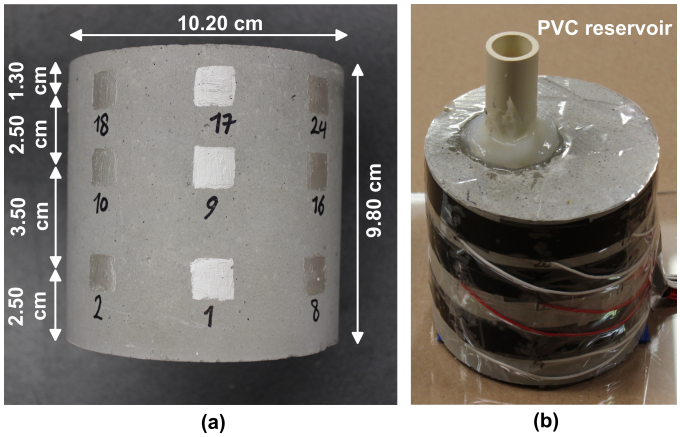

Figure 1: (a) Photograph of the specimen and locations of the electrodes, (b) prepared specimen.

2.2. Materials and sample preparation

The specimens used in this work were made of Portland cement mortar. The mortar was made with ordinary Type I Portland cement and fine aggregate consisting of natural river sand. The water-to-cement ratio (w/c) of the mortar was 0.60 and its total volumetric aggregate content was 40%. The high w/c and low aggregate content (high cement paste content) were used to accelerate the rate of moisture ingress and to reduce the test duration. The mortar mixture was prepared according to ASTM C192-06 [51]. A circular cylinder of diameter 10.20 cm and height 20.30 cm was cast from the mixture. The cylinder was demolded after 18 hours and cut in half to create the two specimens for the experiments.

After cutting, the specimen was moved to an oven at 50°C for 5 hours, and then sealed in two layers of plastic bags and placed inside an environmental chamber at 23°C for 21 days. This process was carried out to achieve a relatively uniform moisture content throughout the specimen. The uniform initial moisture content was not necessary for EIT measurements, but was considered to improve the contrast in X-ray CT images. Furthermore, the corroboration of the experimental results with the flow simulation required the knowledge of the initial moisture content. The initial moisture content was determined experimentally by completely drying separate specimens conditioned using the same procedure; the conditioning resulted in an initial moisture content of $\theta_i = 0.07$.

The electrodes used in this work were made of colloidal silver paint which was applied to the surface of the specimen using a small brush. The colloidal silver paint had a low resistivity and was fast drying [52]. A total of 24 square electrodes (with dimensions of 1.30 cm $\times$ 1.30 cm) were painted on the perimeter of the specimen. The electrodes were arranged in 3 rings of 8 equally spaced electrodes. Fig. 1a shows the specimen and the locations of the electrodes. After the silver paint had dried, an 18 gage wire was placed on the surface of the silver paint. Contact between the electrodes and wires was secured using electric tape and zip ties (Fig. 1b).

The water reservoirs were made of 5.0 cm long PVC pipes with internal diameters of 0.95 cm, and they were installed on the top of the specimens using fast-drying silicon-based caulking. The water reservoirs were positioned eccentrically 1.30 cm off-center. The purpose of this positioning was to induce asymmetric moisture ingress in the specimens and realize whether EIT reconstructions can capture the water source location and asymmetric flow within the specimens. After placing the water reservoirs, the cylinders were wrapped with transparent tape to prevent evaporation of water from the specimens' surface during the test (Fig. 1b).

3. Electrical Impedance Tomography (EIT)

3.1. Reconstruction methods in EIT

In Electrical Impedance Tomography (EIT), electric currents are injected into an object through a set of electrodes on the specimen's boundary. Corresponding to each current injection, a set of electrode potentials/potential differences are measured with respect to a common ground or between electrodes. Based on the measured potentials, the distribution of the electrical conductivity inside the object is reconstructed. A variety of methods for the image reconstruction in EIT have been developed [53]. Broadly, two imaging methods are commonly used in EIT: difference and absolute imaging.

In difference imaging, the temporal change of the conductivity distribution is estimated based on a difference between potential measurements corresponding to two states: before and after the change. The difference reconstructions are often relatively tolerant to systematic measurement and modeling errors, because the errors at least partly cancel out in the subtraction of the two data sets. However, in the conventional difference imaging scheme, the non-linear observation model of EIT (see below) is globally linearized; this can result severe bias in the reconstructed conductivity change, especially when the true conductivity change is large and/or if a good approximation for the initial conductivity is not available. In consequence, the linearized difference reconstructions are often only qualitative in nature [29, 50]. In [36], the linearized difference imaging was used for monitoring the water ingress in mortar; severe artifacts were observed, especially when the water ingress had caused a large change in the conductivity of the mortar with respect to the initial state. The problems associated with the linearized difference imaging can be avoided to an extent by using the recently proposed non-linear difference imaging approach [47, 54]. In the present study, however, absolute EIT imaging is used – aiming at quantitative reconstructions of the conductivity distributions.

In absolute imaging, the conductivity distribution is reconstructed by solving the full non-linear inverse problem of EIT. The absolute reconstruction usually requires iterative solution. Furthermore, unlike in difference imaging, the reconstructions are generally severely intolerant to modeling errors, and hence, accurate (and computationally expensive) numerical models are needed for modeling the measurements. Consequently, the computational cost of absolute EIT imaging is often significantly higher than that of difference imaging.

In this work, the EIT measurements are modeled by the Complete Electrode Model (CEM), which is the most accurate forward model in EIT to date [55, 56]. The CEM consists of the partial differential equation

$$\nabla \cdot (\sigma \nabla u) = 0, \quad x \in \Omega \tag{1}$$

and the boundary conditions

$$u + \xi_l \sigma \frac{du}{d\bar{n}} = U_l, \quad x \in e_\ell,\ \ell = 1, \ldots, L \tag{2}$$

$$\sigma \frac{du}{d\bar{n}} = 0, \quad x \in \partial\Omega \backslash \bigcup_{\ell=1}^{L} e_\ell \tag{3}$$

$$\int_{e_l} \sigma \frac{du}{d\bar{n}}\, dS = I_l, \quad \ell = 1, \ldots, L \tag{4}$$

where Ω is the target volume, and $\partial\Omega$ is its boundary, σ is the electrical conductivity, u is the electric potential, $\bar{n}$ is the outward unit normal, e_l is the l^{th} electrode, and ξ_l, U_l and I_l, respectively, are the contact

impedance, electric potential and total current corresponding to e_l. Moreover, the current conservation law must be fulfilled

$$\sum_{l=1}^{L} I_l = 0 \tag{5}$$

and the potential reference level must be fixed, for example by writing

$$\sum_{l=1}^{L} U_l = 0. \tag{6}$$

The forward solution of EIT – computing the electrode potentials U_l, given the electrode currents I_l and the conductivity distribution σ – requires the solution of the CEM (1) - (6). In practice, the solution is approximated numerically, for example by using the Finite Element Method (FEM) [57, 58]. The finite element (FE) approximation was used also in the present work, leading to a numerical model $U(\sigma)$ for the dependence between the electrode potentials and a discretized conductivity distribution σ. Further, assuming an additive Gaussian noise, the observation model for the EIT measurements becomes

$$V = U(\sigma) + e \tag{7}$$

where V is a vector consisting of the measured electrode potentials, and e is the Gaussian-distributed noise $e \sim \mathcal{N}(0, \Gamma_e)$. Here, Γ_e is the noise covariance matrix, which can usually be determined experimentally [59]. In principle, the reconstruction of the discretized conductivity distribution σ can be thought as a non-linear fitting problem spanned by model (7), i.e., finding a vector σ such that the computed voltages $U(\sigma)$ fit to the voltage measurement data V. However, due to properties of the model $U(\sigma)$, this is mathematically an ill-posed inverse problem. This implies that classical solutions – such as the least-squares estimate for σ – are practically always unstable and non-unique [60]. In this work, we adopted the so-called Tikhonov regularization [57] to the solution. Furthermore, we introduced constraints for the conductivity values [47], and estimated the conductivity as

$$\widehat{\sigma} = \underset{\sigma_{\min} \leq \sigma \leq \sigma_{\max}}{\arg\min} \left[\|L_e(V - U(\sigma))\|^2 + p(\sigma) \right] \tag{8}$$

where L_e is the Cholesky factor of the noise precision matrix Γ_e^{-1}, i.e. $L_\mathrm{e}^T L_\mathrm{e} = \Gamma_\mathrm{e}^{-1}$, and $p(\sigma)$ is a regularization function [61]. The function $p(\sigma)$ is formulated such that it penalizes improbable features of σ. For the influence of $p(\sigma)$ on the solution of the inverse problem, see e.g. [62, 63, 61]. In the present study, $p(\sigma)$ was constructed to accommodate the so-called smoothness-promoting regularization, which is particularity applicable to diffusive processes [47], such as moisture flow in porous media. The smoothness-promoting function $p(\sigma)$ can be written as $p(\sigma) = \|L_\sigma \sigma\|^2$, where L_σ is spatially weighted discrete differential operator [64, 60, 65].

The constraints ($\sigma_{\min} \leq \sigma \leq \sigma_{\max}$) were selected based on experimentally determined physical limits for the electrical conductivity. First, the lower bound $\sigma_{\min}$ was chosen to be equal to the conductivity corresponding to the initial moisture content $\theta_\mathrm{i} = 0.07$. This choice was made based on the knowledge that the ingress of moisture does not degrease the conductivity of the mortar. Secondly, the upper bound $\sigma_{\max}$ was chosen to be the electrical conductivity of the saturated material. The experiment for determining $\sigma_{\min}$ and $\sigma_{\max}$ using measurements of variably saturated mortar is reported below in Section 3.3.

The computations were performed using a MATLAB implementation which is an adaption of codes reported in [66, 67]. In the FE approximation of the forward model, a maximum element dimension of 1.75 mm was chosen, resulting in FE meshes with over 946,500 tetrahedral elements. For the Tikhonov regularized solution (8), Gauss-Newton method was used. The computations were performed utilizing parallel computing processes on eight quad-core processors using 32 Gb total memory and implementation of [68] to solve the systems of linear equations.

3.2. EIT measurement strategy

The EIT measurements were carried out using an in-house developed EIT equipment described in [15]. In all measurements, an alternating current with 0.10 mA amplitude and 40.0 kHz frequency was used. This frequency was chosen based on Electrical Impedance Spectroscopy (EIS) measurements; at frequency 40 kHz, the imaginary component of the impedance was at the minimum. The accuracy of the potential measurements was $\pm 1.0 \times 10^{-8}$ V. In the EIT measurements, current was injected between electrodes i and j where $i, j = \{1, ..., 24\}$ and $i \neq j$. Corresponding to each current injection, potential measurements were taken with respect to a common ground. 561 current injections and 4488 potential measurements were taken for each set of EIT measurements.

3.3. Experimental material model of electrical conductivity for variably-saturated mortar

To quantify the moisture content using EIT, we used an experimental model of $\theta = \theta(\sigma)$ that relates the electrical conductivity σ to the volumetric moisture content θ. For this aim, we first determined the relationship between the electrical conductivity and the equilibrium relative humidity RH (i.e., $\sigma = \sigma(RH)$). Secondly, we measured the relationship $\theta = \theta(RH)$ between the volumetric moisture content and the equilibrium relative humidity, and finally, combined these two models to get the function $\theta = \theta(\sigma)$. Note that the dependence of θ on σ (or the converse) in cement-based materials was shown to not exhibit hysteresis in [69].

To experimentally determine $\sigma = \sigma(RH)$, a total of six prismatic, 6.0 mm $\times$ 1.5 mm $\times$ 4.0 mm mortar specimens were cut from a mortar cylinder using a precision diamond saw. Stainless electrodes were mounted to the 1.5 mm $\times$ 4.0 mm surface of the specimens using conductive silver-based epoxy. The specimens were then suspended in an air-tight container containing saturated salt solutions of KCl, NaCl, $Mg(NO_3)_2$, K_2CO_3, and $MgCl_2$ which induce RH conditions of 84.0, 75.3, 52.8, 43.6, and 32.3%, respectively [70, 4]. Another specimen was submerged in water to reach saturation. After 5 days of conditioning, the electrical resistances of the specimens were measured in 24-hour intervals until no change in resistance was observed between three consecutive measurements. The electrical resistance R was then converted to conductivity using the relation $\sigma^{-1} = R\frac{A}{L}$, where A and $L = 6.0$ mm are, respectively, the cross-sectional area and the length of the specimen.

The desorption isotherm, $\theta = \theta(RH)$, was experimentally obtained using an automated sorption analyzer [71, 72]. The function $\theta = \theta(\sigma)$ was then obtained by a piecewise cubic interpolation [73] to the above mentioned experimental data. This interpolation method was selected to (i) create continuity between intermediate values of θ and (ii) preserve the curve shape at high levels of moisture saturation. The experimentally obtained data and fitted curve are shown in Figure 2.

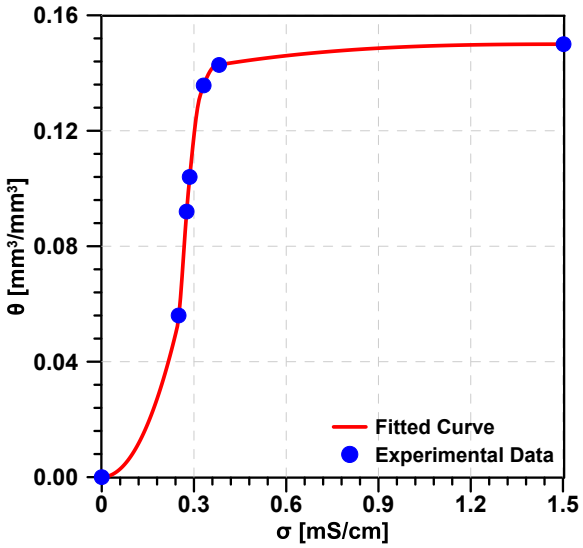

Figure 2: Fitted moisture retention curve for mortar using van Genuchten parameters

Using the initial moisture content $\theta_{\mathrm{i}} = 0.07$, the moisture content at saturation $\theta_{\mathrm{s}} = 0.15$ and the above described model $\theta = \theta(\sigma)$, the minimum and maximum conductivity of the material were computed, resulting in values $\sigma_{\min} = 0.28$ mS/cm and $\sigma_{\max} = 1.5$ mS/cm. These values were used as the lower and upper bound in Eq. (8).

4. X-ray CT imaging

To corroborate EIT reconstructions, X-ray Computed Tomography (CT) imaging was conducted using a full-scale medical CT scanner with a peak beam energy of 120 kV and intensity of 40-200 mA (Fig. 3). In the CT scanner, the X-ray tube rotates perpendicularly to the circular cross-section of the specimen. As the fan beam rotates around the specimen, detectors on the opposite side are activated and measurements are taken. Upon completing a full rotation, the X-ray absorption coefficient $\mu(\mathrm{mm}^{-1})$ is computed in voxels within the measured slice. X-ray radiation transmitted through the specimen is related to μ via the Lambert-Beer law:

$$I_{\mathrm{x}} = I_0 \exp(-\int \mu d\ell) \tag{9}$$

where I_{x} is the intensity of the transmitted X-ray passing through the specimen, I_0 is the incident X-ray intensity, and ℓ is the arc length variable along the line connecting the X-ray source and detector.

The voxel values of the CT images, $\mu - \mu_{\mathrm{water}}$, were normalized by $\mu_{\mathrm{water}} - \mu_{\mathrm{air}}$ to get Hounsfield numbers H is defined by [74]:

$$H = 1000 \times \frac{\mu - \mu_{\mathrm{water}}}{\mu_{\mathrm{water}} - \mu_{\mathrm{air}}}. \tag{10}$$

Further, the spatial distribution of the volumetric moisture content θ was computed from the Hounsfield numbers [75]:

$$\theta = \frac{H_{\mathrm{s}} - H}{1000}, \tag{11}$$

where H_{s} is the Hounsfield value of a saturated material. Here, the value of H_s was taken from H values corresponding to voxels directly below the water reservoir, where the material was assumed to be completely saturated [72, 8].

In this experiment, only the specimen where the absorbed water contained the radiocontrast agent (Iohexol) was imaged with X-ray CT. As pointed out in [36], the sensitivity of CT does not allow for monitoring the absorption of plain water in this medium and geometry. The specimen was scanned at times 1, 2, 4 and 22 hours after the start of the water ingress. 2D slices were taken through the horizontal and vertical cross sections in 0.6 mm slices. CT images were analyzed using digital imaging software [76].

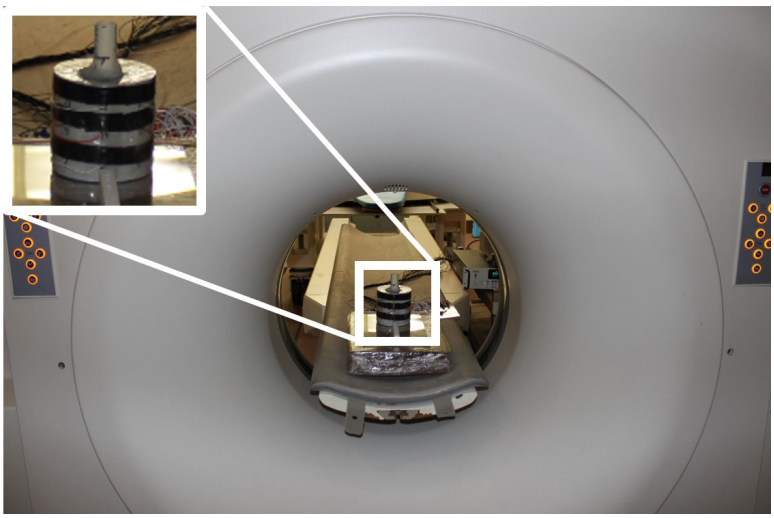

Figure 3: Full-scale medical CT scanner with a peak beam energy of 120 kV and intensity of 40-200 mA testing the specimen used in this study.

5. Numerical simulation of unsaturated moisture flow

5.1. General

Isothermal unsaturated moisture flow in porous media was simulated using Richards' Equation [77, 78]:

$$\frac{\partial \theta}{\partial t} = \frac{\partial}{\partial x}\Big(K(h)\frac{\partial h}{\partial x}\Big) + \frac{\partial}{\partial y}\Big(K(h)\frac{\partial h}{\partial y}\Big) + \frac{\partial}{\partial z}\Big(K(h)\frac{\partial h}{\partial z} + 1\Big) \tag{12}$$

where $K = K(h)$ (mm/hour) is the unsaturated hydraulic conductivity, θ (mm^3/mm^3) is the volumetric moisture content, h (mm) is the pressure head, and x, y, and z (mm) are spatial coordinates. In this work finite element approximation of Eq. (12) was used to simulate the moisture flow in mortar.

5.2. Material model

In general, the unsaturated hydraulic conductivity is expressed as the product of the relative hydraulic conductivity K_r and the saturated hydraulic conductivity K_s, such that $K = K_\mathrm{r}K_\mathrm{s}$. For unsaturated porous media, K_r is described by Mualem's equation [79]:

$$K_r = \Theta^I \left[\frac{\int_0^\Theta \frac{1}{h(x)}, dx}{\int_0^1 \frac{1}{h(x)}, dx}\right]^2 \tag{13}$$

$$\Theta = \frac{\theta - \theta_\mathrm{r}}{\theta_\mathrm{s} - \theta_\mathrm{r}} \tag{14}$$

where $0 \leq \Theta \leq 1.0$ is the effective material saturation, θ_r is the residual moisture content where $\theta_\mathrm{r} = 0$ is generally considered as an appropriate assumption for cement-based materials [72, 7], θ_s is the saturated moisture content that is measured experimentally in this work ($\theta_\mathrm{s} = 0.15$), I is the tortuosity and pore connectivity parameter; in this work $I = -9.0$ is taken from [80]. Discussion of I in cement-based materials is provided in [81] and [82]. In this work, saturated hydraulic conductivity $K_s = 5.0 \times 10^{-3}$ (mm/hr) is obtained experimentally using Darcy's Law and the procedure in [70].

In order to calculate the integrals in Eq. (13), the effective material saturation is expressed as a function of the pressure head, $\Theta = \Theta(h)$ using the van Genuchten model [83, 84]:

$$\Theta = \frac{1}{[1 + (\alpha h)^n]^m}, \quad m = 1 - \frac{1}{n} \tag{15}$$

where α (mm^{-1}) and $n(-)$ are fitting parameters. For cement-based materials, instead of expressing water retention as $\Theta = \Theta(h)$, the material sorption isotherm is generally obtained experimentally as $\Theta = \Theta(RH)$, where RH denotes relative humidity. In this work, the desorption isotherm was experimentally measured using an automated sorption analyzer [71, 72] (see Section 3.3) For simplicity we neglected the effect of hysteresis. To convert the experimentally obtained isotherm $\Theta(RH)$ to the moisture retention curve as $\Theta(h)$, the Kelvin-Laplace Equation is used [7, 85]:

$$h = \frac{\rho_{\mathrm{w}} R_{\mathrm{s}} T}{m_{\mathrm{w}}} \ln(RH) \tag{16}$$

where ρ_{w} ($\mathrm{g/mm}^3$) is the density of water, R_{s} (8.845 $\mathrm{JK}^{-1}\mathrm{mol}^{-1}$) is the universal gas constant, and m_w (g/mol) is the molecular weight of water. By fitting the model in Eq. (15) to the water retention curve $\Theta(h)$, van Genuchten parameters $\alpha = 2.63 \times 10^{-2}$ (mm^{-1}) and $n = 1.77$ were obtained. The experimentally obtained data points and the fitted van Genuchten model are shown in Figure 4.

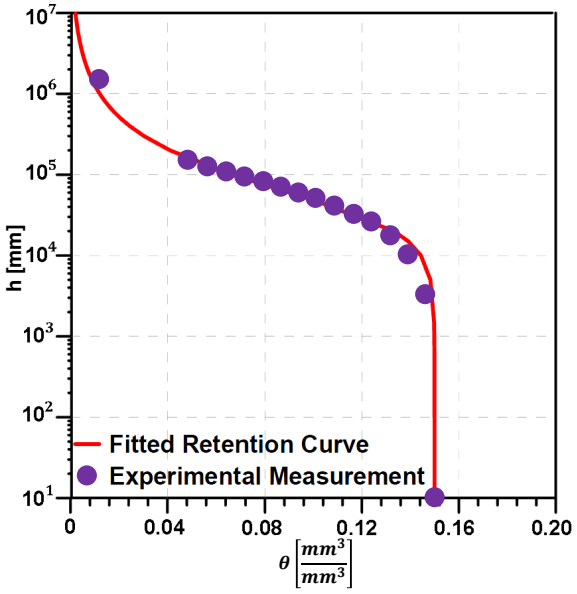

Figure 4: Fitted moisture retention curve for mortar using van Genuchten parameters

5.3. Simulation of moisture flow

The moisture flow in the specimen was modeled using a commercially available Finite Element Software HYDRUS 3D [86]. Zero-flux boundary conditions were considered at all surfaces except the surface from which water penetrated (water reservoir), which was modeled as a 9.5 mm diameter circle saturated throughout the simulation. Uniform initial moisture content, $\theta_{\mathrm{i}} = 0.07$ was selected based on the experiments described in Section 2.2. The Finite element mesh consisted of tetrahedral elements with a maximum dimension of 4 mm. The finite element model was solved in terms of moisture content.

6. Results and discussion

Figures 5 and 6 show the results of the experiment where the dilute solution of water and Iohexol was absorbed to a mortar specimen. The left column of Fig. 5 illustrates the 3D electrical conductivity distribution reconstructed based on EIT measurements after 1, 2, 4 and 22 hours of moisture penetration. In the images, the black rectangles mark the electrodes attached on the surface of the specimen. The series of EIT reconstructions clearly shows the ingress of moisture: After 1 hour of moisture ingress, a small volume directly under the water reservoir features increase of the electrical conductivity; in the subsequent time intervals, the volume with increased conductivity gets larger. Also the value of the conductivity under the

water reservoir increases over time, being close to conductivity at saturation, $\sigma_s = 1.5$ mS/cm, after 22 hours of moisture ingress.

The EIT-based estimates for the 3D volumetric moisture content θ at times 1, 2, 4 and 22 hours are shown in the right column of Fig. 5. These moisture content estimates were computed from the reconstructed 3D conductivity distributions σ using the experimentally developed model $\theta = \theta(\sigma)$ described in Section 3.3. While the reconstructed conductivity distributions in the left column illustrate the ingress of moisture through the specimen qualitatively, the 3D volumetric moisture content estimates allow for quantifying the moisture ingress. For example, the reconstructions of θ show that the moisture content is approximately 0.12 directly below the water reservoir after 1 hour of moisture ingress, and is nearly saturated ($\theta_s = 0.15$) after 22 hours of moisture ingress, while the background moisture content remains at the initial value 0.07. Qualitatively, the spatial and temporal gradients of θ look somewhat different from those of σ. This difference results from the non-linearity of the model $\sigma = \sigma(\theta)$.

The left column of Fig. 6 represents the EIT-based reconstructions of the 3D volumetric moisture content θ on a vertical 2D plane crossing the center of the water reservoir and extending to the exterior of the specimen. The right column shows X-ray CT images at the respective times. In these images, the water reservoir appears in the center of the top surface, because the 2D slice crossing the center of the water reservoir is off-centric with respect to the specimen; this is due to the orientation of the sample during the CT scan (Fig. 3). Also the X-ray CT images show the increase of θ directly below the water reservoir, and the value of θ in this region is close to the saturation value 0.15 at times 1 h and 2 h. However, in the 4 h and 22 h CT images, the value of the moisture content has decreased under the water reservoir, indicating a low sensitivity of CT to the water content with this specimen size. Moreover, the X-ray CT images presented here detect only high levels of saturation (similarly to X-ray images in [7]). The CT images do not show the presence of low levels of saturation because of the large sample size used (10.20 cm$\times$ 20.30 cm cylinder). Some previous studies using X-ray imaging (e.g, [9] and [10]) showed high resolution images of unsaturated moisture flow in cement-based material; however, the specimen sizes were small (maximum dimension of 5.5 cm in cement-based specimen tested). These results demonstrate that EIT is capable of imaging the moisture flow in a specimen, the size of which exceeds the limit of a regular CT scanner.

Figure 7 shows the results corresponding to the experiment where plain water was absorbed into a mortar specimen. The left column illustrates the volumetric moisture content θ reconstructed using EIT, and the right column shows θ computed by moisture flow simulation specified in Section 5.3. All images represent the vertical 2D cross-sections of the corresponding 3D distributions. The EIT reconstructions show a good correspondence with the moisture flow simulation. Indeed, the ingress of moisture predicted by the flow simulation is captured well by EIT, and the size and shape of the (nearly) saturated volume $\theta \approx 0.15$ in EIT-based images are close to those in the simulation-based images. Also the shapes of intervals with lower saturation in EIT-based reconstructions of θ compare relatively well with those in the simulations.

The addition of the radiocontrast agent (Iohexol) increases the viscosity and surface tension of water, and thus, the flow of the diluted solution in porous media is slower than the flow of plain water. The capability of EIT to distinguish between flow rates of these two liquids was shown in [36]. The comparison between the left columns of Figs. 6 and 7 further confirms this; especially, the volume of the saturated mortar is consistently larger in Fig. 7 than in the respective times in Fig. 6.

7. Summary and conclusions

In this paper, we investigated whether Electrical Impedance Tomography (EIT) could be used to quantitatively monitor 3D moisture flow in cement-based materials. For this aim, we conducted an experiment where mortar specimens were imaged with EIT during the ingress of moisture. The so-called absolute imaging scheme was used to reconstruct the 3D distributed electrical conductivity within the mortar. The reconstructed electrical conductivity distributions were further converted to volumetric moisture content distributions, by using an experimentally-developed model. One of the samples was simultaneously imaged by a regular X-ray CT scan. Moreover, the results of EIT were corroborated by a numerical simulation of unsaturated moisture flow.

EIT captured the moisture flow in mortar and provided quantitative information on volumetric moisture content. The EIT-based estimates for the moisture content compared well with numerical simulations of unsaturated moisture flow. In contrast to X-ray CT images, which showed only highly saturated material,

EIT reconstructions provided a good resolution at various levels of saturation. In the previous work [36], the difference imaging scheme was used to visualize moisture flow in cement-based materials, and significant artifacts were observed at the late stages of moisture flow. In the present work, however, the use of application-specific absolute imaging eliminated the artifacts in the reconstructions at late stages of moisture ingress, since, unlike difference imaging, absolute imaging is not based on the assumption of small changes in the electrical conductivity with regards to a reference state. Based on these findings, EIT shows promise for becoming a tool for imaging moisture flow in cement-based materials non-destructively and quantitatively. Moreover, the developed procedure for quantifying the moisture content using EIT is also applicable for other porous media.

Acknowledgements

This work was conducted in the Materials and Sensor Development Laboratory (MSDL) and Constructed Facilities Laboratory (CFL) at North Carolina State University (NCSU). The third author would like to acknowledge the support provided by Academy of Finland (projects 270174 and 273536). The authors would like to acknowledge the support which has made these laboratories and this research possible. The authors also thank the technical support of these laboratories. The authors greatly acknowledge the expertise of Dr. Gary Howell and Dr. Jianwei Dian at NCSU High-Preformance Computing (HPC) for the technical assistance in implementing the Load Sharing Facility HPC environment used to compute the image reconstructions in this study. The authors would like to thank Dr. Ian Robertson from the NCSU College of Veterinary Medicine (CVM) for his assistance in using X-ray Computed Tomography facilities. All support is greatly appreciated and acknowledged.

References

[1] L. Dormieux, D. Kondo, F. Ulm, Microporomechanics, 1st Edition, John Wiley & Sons, West Sussex, England, 2006.

[2] C. Hall, W. Hoff, Water transport in brick, stone, and concrete, London and New York, 2002.

[3] J. Bear, Dynamics of fluids in porous media, 2nd Edition, Dover Publications, Inc., New York, 1988.

[4] J. Castro, D. Bentz, J. Weiss, Effect of sample conditioning on the water absorption of concrete, Cement Concrete Comp. 33 (8) (2011) 805–813.

[5] W. D. Lindquist, D. Darwin, J. Browning, G. G. Miller, Effect of cracking on chloride content in concrete bridge decks, ACI Mater. J. 103 (6) (2006) 467–473.

[6] J. Daïan, J. Salbia, Transient moisture transport in a cracked porous medium, Transport Porous Med. 13 (1993) 239–260.

[7] M. Pour-Ghaz, F. Rajabipour, J. Couch, J. Weiss, Numerical and experimental assessment of unsaturated fluid transport in saw-cut (notched) concrete elements, ACI Special Publication 266 (2009) 73–86.

[8] M. Pour-Ghaz, F. Rajabipour, J. Couch, J. Weiss, Modeling fluid transport in cementitious systems with crack-like (notch) geometries, International RILEM Workshop on Concrete Durability and Service Life Planning. Haifa, Israel 2009 (2009) 71–79.

[9] S. Roels, J. Carmeliet, Analysis of moisture flow in porous materials using microfocus X-ray radiography, Int. J. Heat Mass Transf. 49 (25-26) (2006) 4762–4772.

[10] S. Roels, J. Carmeliet, H. Hens, O. Adan, H. Brocken, R. Cerny, Z. Pavlik, A. Ellis, C. Hall, K. Kumaran, A comparison of different techniques to quantify moisture content profiles in porous building materials, J. Thermal Env. and Bldg. Sci. 27 (4) (2004) 261–276.

[11] C. Dierke, U. Werban, Relationships between gamma-ray data and soil properties at an agricultural test site, Geoderma 199 (2013) 90–98.

[12] M. Nizovtsev, S. Stankus, A. Sterlyagov, V. Terekhov, R. Khairulin, Determination of moisture diffusivity in porous materials using gamma-method, Int. J. Heat Mass Transf. 54 (17-18) (2008) 4161–4167.

[13] A. Nielsen, Gamma-ray-attenuation used for measuring the moisture content and homogeneity of porous concrete, Build. Sci. 7 (4) (1972) 257–263.

[14] W. Li, M. Pour-Ghaz, P. Trtik, M. Wyrzykowski, B. Münch, P. Lura, P. Vontobel, E. Lehmann, W. J. Weiss, Using neutron radiography to assess water absorption in air entrained mortar, Const Build Mater 110 (2016) 98 – 105.

[15] M. Hallaji, A. Seppänen, M. Pour-Ghaz, Electrical resistance tomography to monitor unsaturated moisture flow in cementitious materials, Cement and Concrete Res. 69 (2015) 10–18.

[16] P. Zhang, F. H. Wittmann, T. Zhao, E. H. Lehmann, P. Vontobel, Neutron radiography, a powerful method to determine time-dependent moisture distributions in concrete, Nucl. Eng. and Des. 241 (12) (2011) 4758–4766.

[17] P. Zhang, F. Wittmann, T. Zhao, E. Lehmann, Neutron imaging of water penetration into cracked steel reinforced concrete, Physica B. 405 (7) (2010) 1866–1871.

[18] M. Kanematsu, I. Maruyama, T. Noguchi, H. Iikura, T. N., Quantification of water penetration into concrete through cracks by neutron radiography, Nucl. Instrum. Methods Phys. Res. Sect. A. 605 (1-2) (2009) 154–158.

[19] M. Zreda, D. Desilets, T. Ferré, R. Scott, Measuring soil moisture content non-invasively at intermediate spatial scale using cosmic-ray neutrons, Geophys. Res. Lett. 35 (2008) doi:10.1029/2008GL035655.

[20] M. Deinert, J. Parlange, T. J. Steenhuis, T., K. Ünlü, K. Cady, Measurement of fluid contents and wetting front profiles by real-time neutron radiography, J. of Hydrol. 290(3-4) (2004) 191–201.

[21] W. McCarter, D. Watson, Wetting and drying of coverzone concrete, in: Inst. Civ. Eng. Struct. Build., Vol. 112, 1997, pp. 227–236.

[22] W. McCarter, Monitoring the influence of water and ionic ingress on cover zone concrete subjected to repeated absorption, Cement Concrete Aggr. 18 (1) (1996a) 55–63.

[23] W. McCarter, H. Ezirim, M. Emerson, Properties of concrete in the cover zone: Water penetration, sorptivity, and ionic ingress, Mag. Concrete Res. 48 (176) (1996b) 149–156.

[24] S. Merz, A. Polhmeier, J. Vanderborght, D. van Dusschoten, H. Vereecken, Moisture profiles of the upper soil layer during evaporation monitored by NMR, Water Resour. Res. 50(6) (2014) 51845195.

[25] J. Perlo, E. Danieli, J. Perlo, B. Blümich, F. Casanova, Optimized slim-line logging NMR tool to measure soil moisture in situ, J. of Mag. Res. 233 (2013) 74–79.

[26] C. Hall, W. Hoff, Water transport in brick, stone and concrete, 2nd Edition, Taylor & Francis, London and New York, 2012.

[27] Q. Chen, M. Gingras, B. Balcom, A magnetic resonance study of pore filling processes during spontaneous imbibition in Berea sandstone, J. Chem. Phys. 119 (18) (2003) 9609–9616.

[28] R. Gummerson, C. Hall, W. Hoff, R. Hawkes, G. Holland, W. Moore, Unsaturated water flow within porous materials observed by NMR imaging, Nature 281 (1979) 56–57.

[29] M. Hallaji, Monitoring damage and unsaturated moisture flow in concrete with electrical resistance tomography (ERT), Ph.D. thesis, North Carolina State University, Raleigh, North Carolina (2015).

[30] W. McCarter, T. Chrisp, G. Starrs, A. Adamson, E. Owens, P. Basheer, S. Nanukuttan, S. Srinivasan, N. Holmes, Developments in performance monitoring of concrete exposed to extreme environments, J. Infrastruct. Syst. 18 (3) (2012) 167–175.

[31] Z. Liu, J. J. Beaudoin, An assessment of the relative permeability of cement systems using AC impedance techniques, Cem. Concr. Res. 29 (7) (1999) 1085–1090.

[32] Z. Xu, P. Gu, P. Xie, J. J. Beaudoin, Application of AC impedance techniques in studies of porous cementitious materials: (II): Relationship between ACIS behavior and the porous microstructure, Cem. Concr. Res. 23 (4) (1993) 853–862.

[33] P. Gu, P. Xie, J. J. Beaudoin, R. Brousseau, AC impedance spectroscopy (II): Microstructural characterization of hydrating cement-silica fume systems, Cem. Concr. Res. 23 (1) (1993) 157–168.

[34] P. Gu, Z. Xu, P. Xie, J. J. Beaudoin, Application of AC impedance techniques in studies of porous cementitious materials: (I): Influence of solid phase and pore solution on high frequency resistance, Cem. Concr. Res. 23 (3) (1993) 531–540.

[35] P. Gu, P. Xie, J. J. Beaudoin, R. Brousseau, AC impedance spectroscopy (I): A new equivalent circuit model for hydrated portland cement paste, Cem. Concr. Res. 22 (5) (1992) 833–840.

[36] D. Smyl, M. Hallaji, A. Seppänen, M. Pour-Ghaz, Three-dimensional electrical impedance tomography to monitor unsaturated moisture ingress in cement-based materials, Transport Porous Med. (Accepted).

[37] R. Du Plooy, G. Villain, S. Palma Lopes, A. Ihamouten, X. Dérobert, B. Thauvin, Electromagnetic non-destructive evaluation techniques for the monitoring of water and chloride ingress into concrete: a comparative study, Mater. Struct. 48 (1) (2015) 369–386.

[38] R. M. Cosentini, G. Della Vecchia, S. Foti, G. Musso, Estimation of the hydraulic parameters of unsaturated samples by electrical resistivity tomography, Géotechnique 62 (7) (2012) 583–594.

[39] C. Comina, R. M. Cosentini, G. Della Vecchia, S. Foti, G. Musso, 3D-electrical resistivity tomography monitoring of salt transport in homogeneous and layered soil samples, Acta Geotech. 6 (4) (2011) 195–203.

[40] C. Comina, R. Cosentini, G. Della Vecchia, S. Foti, G. Musso, Hydrochemomechanical processes in soil samples: monitoring through electrical resistivity tomography, in: EPJ Web of Conferences, Vol. 6, EDP Sciences, 2010, p. 22012.

[41] A. Borsic, C. Comina, S. Foti, R. Lancellotta, G. Musso, Imaging heterogeneities with electrical impedance tomography: laboratory results, Géotechnique 55 (7) (2005) 539–547.

[42] W. Daily, A. Ramirez, A. Binley, S. Henry-Poulter, Electrical resistance tomography of concrete structures, in: ECAPT94: 3rd European concerted action meeting on process tomography, Lisbon, Portugal, 1994.

[43] M. Buettner, A. Ramirez, W. Daily, Electrical resistance tomography for imaging the spatial distribution of moisture in pavement sections, in: Structural materials technology an NDT Conference, San Diego, California, 1996.

[44] F. Haegel, E. Zimmerman, O. Esser, K. Breede, J. Huisman, W. Glaas, J. Berwix, H. Vereecken, Determination of the distribution of air and water in porous media by electrical impedance tomography and magneto-electrical imaging, Nuc. Eng. D. 241 (2011) 1959–1969.

[45] R. Stacey, Electrical impedance tomography, geothermal program interdisciplinary research in engineering and earth sciences, Tech. Rep. SGP-TR-182, Stanford University (2006).

[46] O. Kuras, J. Pritchard, P. Meldrum, J. Chambers, P. Wilkinson, R. Ogilvy, G. Wealthall, Monitoring hydraulic processes with automated time-lapse electrical resistivity tomography (ALERT), Appl. Geophys. 341 (2009) 868–885.

[47] D. Liu, V. Kolehmainen, S. Siltanen, A. Laukkanen, A. Seppänen, Estimation of conductivity changes in a region of interest with electrical impedance tomography, Inverse Probl. Imag. 9(1) (2015) 211–229.

[48] P. Vauhkonen, Image reconstruction in three-dimensional electrical impedance tomography, Ph.D. thesis, University of Kuopio (2004).

[49] B. Brown, Electrical impedance tomography (EIT): a review, J. Med. Eng. Technol. 27 (2003) 97–108.

[50] M. Vauhkonen, Electrical impedance tomography and prior information, Ph.D. thesis, University of Kuopio (1997).

[51] ASTM, Standard practice for making and curing concrete test specimens in the laboratory (2006).

[52] M. Pour-Ghaz, Detecting damage in concrete using electrical methods and assessing moisture movement in cracked concrete, Ph.D. thesis, Purdue University, Indiana (2011).

[53] L. Borcea, Electrical impedance tomography, Inverse Probl. 18 (2002) R99–R136.

[54] D. Liu, V. Kolehmainen, S. Siltanen, A. Seppänen, A nonlinear approach to difference imaging in EIT; assessment of the robustness in the presence of modelling errors, Inverse Problems 31 (3) (2015) 035012.

[55] E. Somersalo, M. Cheney, D. Isaacson, Existence and uniqueness for electrode models for electric current computed tomography, SIAM Jour. on Appl. Math. 52 (4) (1992) 1023–1040.

[56] K.-S. Cheng, D. Isaacson, J. Newell, D. Gisser, Electrode models for electric current computed tomography, IEEE T. Bio-Med. Eng. 36 (9) (1989) 918–924.

[57] M. Vauhkonen, W. Lionheart, L. Heikkinen, P. Vauhkonen, J. Kaipio, A MATLAB package for the EIDORS project to reconstruct two-dimensional EIT images, Physiol. Meas. 22 (2001) 107–111.

[58] P. J. Vauhkonen, M. Vauhkonen, T. Savolainen, J. P. Kaipio, Three-dimensional electrical impedance tomography based on the complete electrode model, IEEE T. Biomedical Eng. 46(9) (1999) 1150–1160.

[59] L. M. Heikkinen, T. Vilhunen, R. M. West, M. Vauhkonen, Simultaneous reconstruction of electrode contact impedances and internal electrical properties: II. laboratory experiments, Measurement Science and Technology 13 (12) (2002) 1855.

[60] J. Kaipio, E. Somersalo, Statistical and Computational Inverse Problems, Springer New York, 2005.

[61] M. Vauhkonen, P. Vadász, E. Karjalainen, E. Somersalo, J. Kaipio, Tikhonov regularization and prior information in electrical impedance tomography, IEEE transactions on medical imaging 17(2) (1998) 285–293.

[62] M. Heidary-Fyrozjaee, Control of displacement fronts in porous media by flow rate partitioning, Ph.D. thesis, University of Southern California, Los Angeles, CA (2008).

[63] A. Beck, A. Ben-tal, On the solution of the Tikhonov regularization of the least squares problem, SIAM J. of Optimiz. 17(1) (2006) 98–118.

[64] N. Hyvönen, A. Seppänen, S. Staboulis, Optimizing electrode positions in electrical impedance tomography, SIAM J. of Appl. Math. 74(6) (2014) 1831–1851.

[65] J. Kaipio, V. Kolehmainen, M. Vauhkonen, E. Somersalo, Inverse problems with structural prior information, Inverse Probl. 15 (1999) 713–729.

[66] A. Adler, W. R. Lionheart, Uses and abuses of EIDORS: an extensible software base for EIT, Physiol. Meas. 27 (5) (2006) S25.

[67] N. Polydorides, W. Lionheart, A MATLAB toolkit for three-dimensional electrical impedance tomography: a contribution to the electrical impedance and diffuse optical reconstruction software project, Meas. Sci. Technol. 13 (12) (2002) 1871–1883.

[68] J. W. Demmel, J. R. Gilbert, X. S. Li, An asynchronous parallel supernodal algorithm for sparse gaussian elimination, SIAM J. Matrix Anal. A. 20(4) (1999) 915–952.

[69] F. Rajabipour, J. Weiss, Electrical conductivity of drying cement paste, Mater. Struct. 40 (2007) 1143–1160.

[70] F. Ghasemzadeh, M. Pour-Ghaz, The effect of damage on moisture transport in concrete, J. Mat. Civil Eng. (2014) DOI: 10.1061/(ASCE)MT.1943–5533.0001211.

[71] C. Villani, R. Spragg, M. Pour-Ghaz, J. Weiss, The influence of pore solutions properties on drying in cementitious materials, J. of the Am. Ceram. Soc. 97 (2014) 386–393.

[72] M. Pour-Ghaz, R. Spragg, J. Weiss, Moisture profiles and diffusion coefficients in mortars containing shrinkage reducing admixtures, International RILEM Conference on Use of Superabsorbent Polymers and Other New Additives in Concrete Technical University of Denmark (2010) 197–206.

[73] F. Fritsch, R. Carlson, Monotone piecewise cubic interpolation, SIAM J. of Numer. Anal. 17(2) (1979) 238–246.

[74] T. Feeman, The Mathematics of Medical Imaging, 1st Edition, Springer Science, LLC., New York, 2010.

[75] I. Tiana, R. Heck, T. Elliot, Application of X-ray computed tomography to soil science:a literature review, Can. J. of Soil Sci. 88(1) (2007) 1–20.

[76] M. Abramoff, P. Magalhaes, S. Ram, Image processing with ImageJ, Biol. Med. Phys. Biomed. 11(7) (2004) 36–42.

[77] F. E. Botros, Y. S. Onsoy, T. R. Ginn, T. Harter, Richards equation–based modeling to estimate flow and nitrate transport in a deep alluvial vadose zone, Vadose Zone J. 11 (4).

[78] L. A. Richards, Capillary conduction of liquids through porous mediums, Physics 1(5) (1931) 318–333.

[79] Y. Mualem, A new model for predicting the hydraulic conductivity of unsaturated porous media, Water Resour. Res. 12(3) (1976) 513–522.

[80] D. Smyl, F. Ghasemzadeh, M. Pour-Ghaz, Modeling water absorption in concrete and mortar with distributed damage, Construction and Building Materials. (Accepted).

[81] M. Auroy, S. Poyet, P. Le Bescop, J. M. Torrenti, T. Charpentier, M. Moskura, X. Bourbon, Impact of carbonation on unsaturated water transport properties of cement-based materials, Cement Concrete Res. 74 (2015) 44–58.

[82] S. Poyet, S. Charles, N. Honore, V. L'hostit, Assessment of unsaturated water transport properties in an old concrete: determination of the pore-interaction factor, Cement and Concrete Res. 41(10) (2011) 1015–1023.

[83] M. T. van Genuchten, A closed-form equation for predicting the hydraulic conductivity of unsaturated soils, Soil Sci. Soc. Am. J. 44 (1980) 892–898.

[84] M. T. van Genuchten, D. R. Nielson, On describing and predicting the hydraulic properties of unsaturated soils, Ann. of Geophys. 3 (1985) 615–628.

[85] C. Leech, D. Lockington, R. Hooton, G. Galloway, G. Cowin, P. Dux, Validation of Mualem's conductivity model and prediction of saturated permeability from sorptivity, ACI Mater. J. 105 (1) (2008) 44–51.

[86] J. Šimůnek, M. T. van Genuchten, M. Šejna, Development and applications of the HYDRUS and STANMOD software packages and related codes, Vadose Zone J. 7 (2) (2008) 587–600.

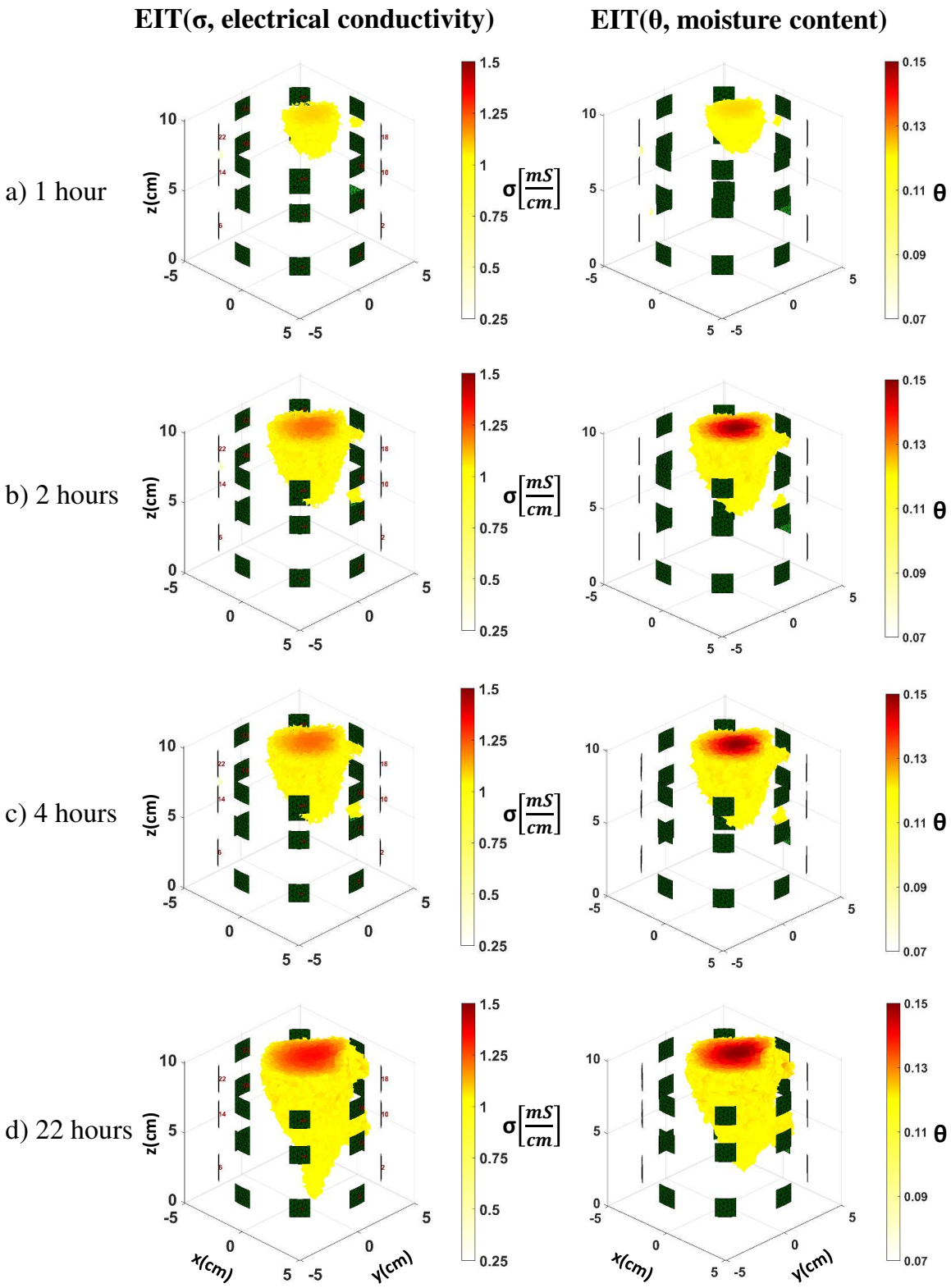

Figure 5: Results of the experiment with dilute solution of water and Iohexol; 3D EIT reconstructions depicting electrical conductivity (σ, left column) and volumetric moisture content (θ, right column) for moisture ingress at: (a) 1 hour, (b) 2 hours, (c) 4 hours (d) 22 hours.

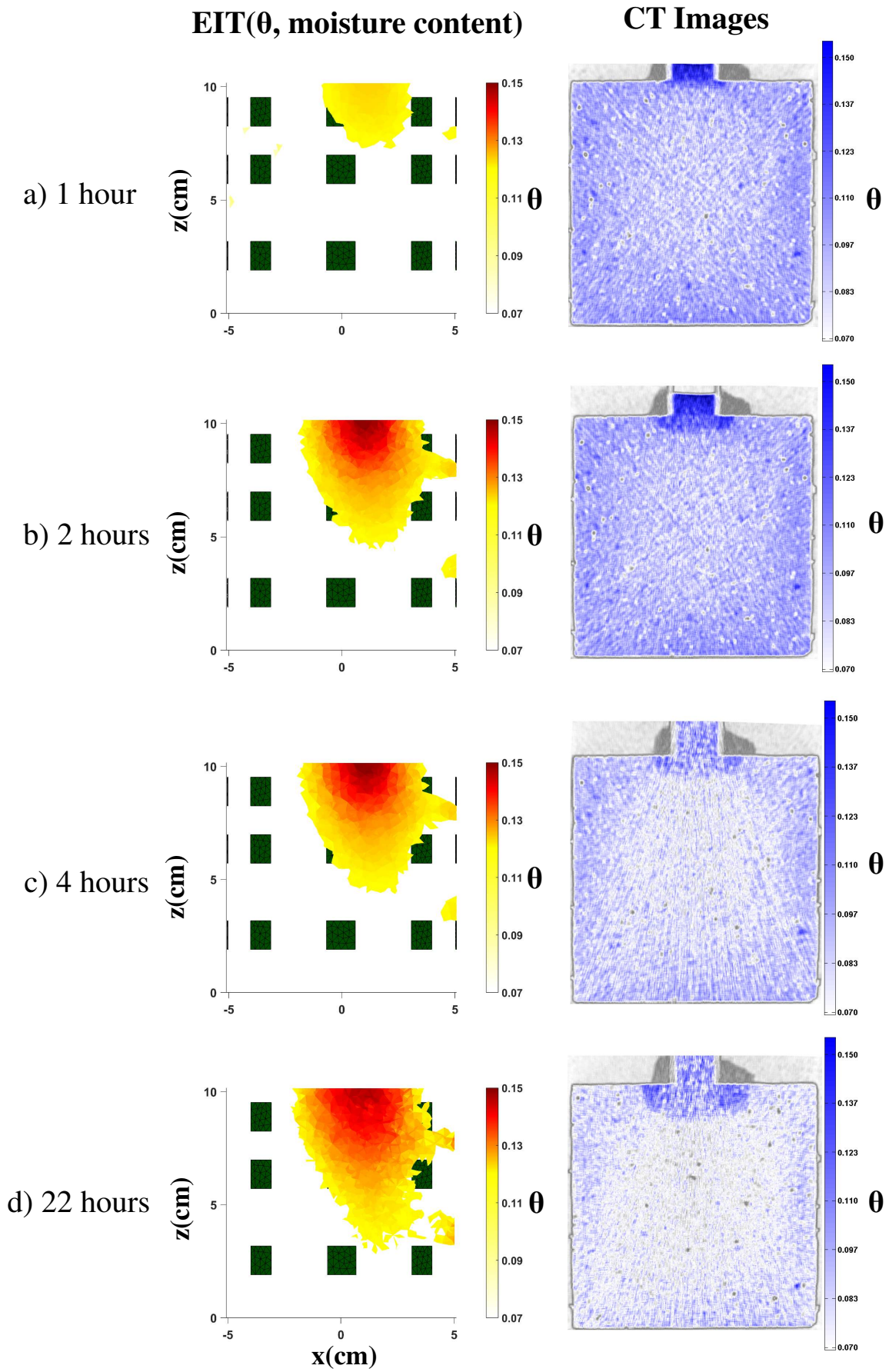

Figure 6: Results of the experiment with dilute solution of water and Iohexol; 2D slices of the EIT-based 3D reconstructions of the volumetric moisture content (left column) and CT-based images of the volumetric moisture content (right column) at: (a) 1 hour, (b) 2 hours, (c) 4 hours (d) 22 hours

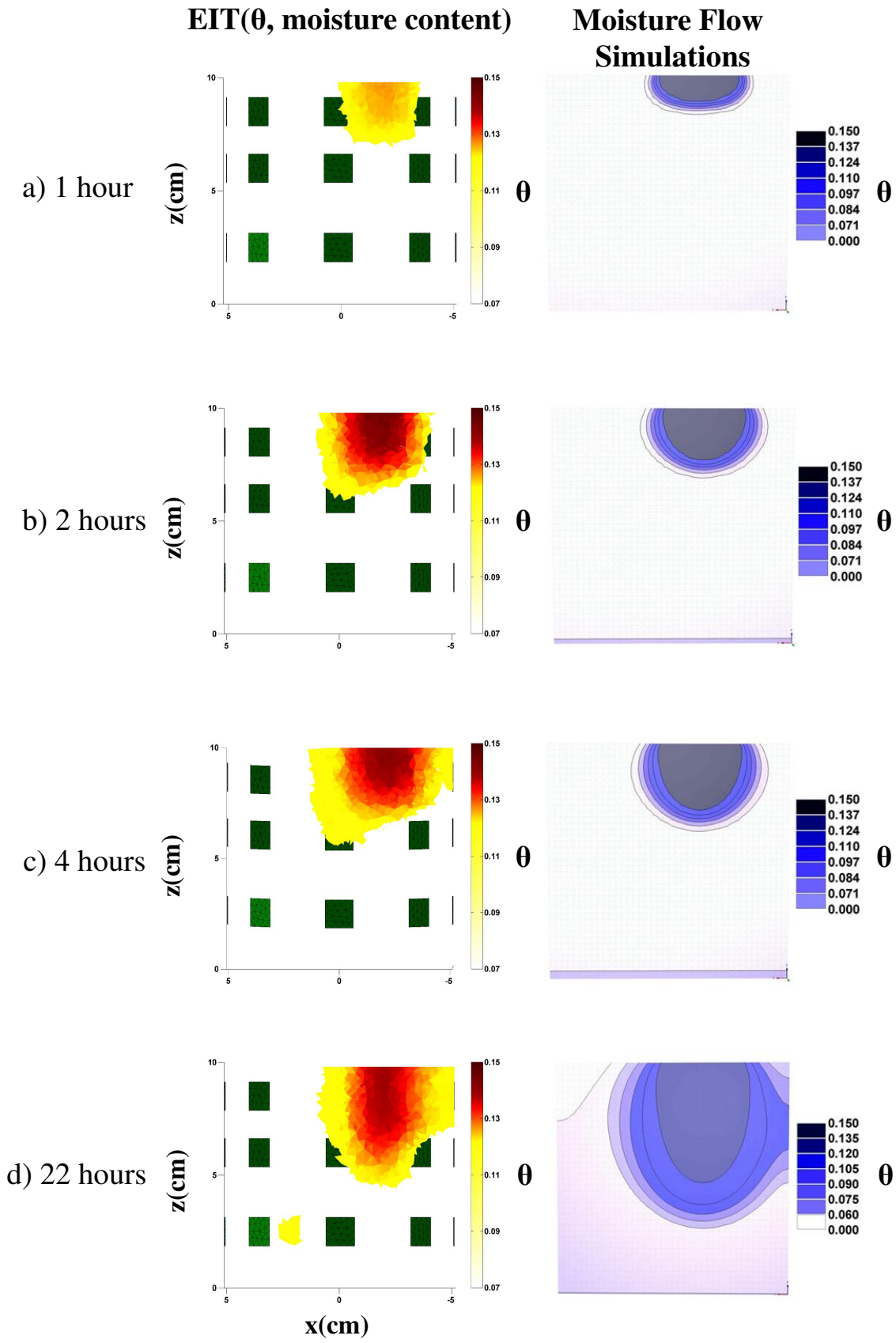

Figure 7: Results of the experiment with plain water; 2D slices of the EIT-based 3D reconstructions of the volumetric moisture content (left column) and moisture flow simulation -based images of the volumetric moisture content (right column) at: (a) 1 hour, (b) 2 hours, (c) 4 hours (d) 22 hours